Title

A Generalized Approach for Reconstructing the Three-Dimensional Shape of Slender Structures Including the Effects of Curvature, Shear, Torsion, and Elongation

Journal

Journal of Applied Mechanics, 84(4)

ISSN

0021-8936

Authors

Chadha, Mayank
Todd, Michael D

Publication Date

2017-04-01

DOI

10.1115/1.4035785

Peer reviewed

A Generalized Approach for Reconstructing the Three-Dimensional Shape of Slender Structures Including the Effects of Curvature, Shear, Torsion, and Elongation

Mayank Chadha
Department of Structural Engineering,
University of California San Diego,
9500 Gilman Drive 0085,
La Jolla, CA 92093-0085
e-mail: machadha@ucsd.edu

Michael D. Todd[1]
Department of Structural Engineering,
University of California San Diego,
9500 Gilman Drive 0085,
La Jolla, CA 92093-0085
e-mail: mdtodd@ucsd.edu

This paper extends the approach for determining the three-dimensional global displaced shape of slender structures from a limited set of scalar surface strain measurements. It is an exhaustive approach that captures the effect of curvature, shear, torsion, and elongation. The theory developed provides both a determination of the uniaxial strain (in a given direction) anywhere in the structure and the deformed shape, given a set of strain values. The approach utilizes Cosserat rod theory and exploits a localized linearization approach that helps to obtain a local basis function set for the displacement solution in the Cosserat frame. For the assumed deformed shape (both the midcurve and the cross-sectional orientation), the uniaxial value of strain in any given direction is obtained analytically, and this strain model is the basis used to predict the shape via an approximate local linearized solution strategy. Error analysis due to noise in measured strain values and in uncertainty in the proximal boundary condition is performed showing uniform convergence with increased sensor count. [DOI: 10.1115/1.4035785]

Keywords: shape sensing, Cosserat beam theory, directors, material frame, local basis function

1 Introduction

This paper extends the theory of shape sensing from strain measurements presented by Todd et al. [1]. Unlike Ref. [1], which uses a relationship between a Frenet coordinate system and a body-centered coordinate system on an unsheared cross section, we directly exploit the body-centered material frame in a way that captures the complete effects of multiple curvatures, shear, elongation, and torsion, consistent with the Cosserat theory. We assume the cross-sectional shape to be geometrically unchanged after deformation, and thus, we ignore Poisson's and warping effects in the present study.

There are multiple instances where it is desirable to reconstruct the full-field deformed shape of a very long, slender object, such as pipelines, suspension cables, tethers, surgical tubing, catheters, and others. In the present work, the inclusive consideration of shear effects extends the validity of the proposed approach to even more moderately slender objects like beams or connecting rods while generally providing robustness in the predicted results. This theory mainly targets the set of structures that are subjected to small strains (elastic response) but arbitrarily large deformations, such a scenario occurs in such essentially one-dimensional structures, implying that the cross-sectional dimension is much smaller than its length [2]. The work on the theory of geometrically exact beams was mainly contributed by Timoshenko, Iura and Atluri [3], Simo and Vu-Quoc [4], and Reissner [5–7], which are all based on the work of Euler beam theory, with more modern work by Kirchhoff, Love [8], and most importantly by Cosserat and Cosserat [9]. There is substantial literature on Cosserat theories including that by Rubin [10–12]. All these approaches model the kinematic deformations directly rather than through traditional elasticity.

This paper infers the global displacement (defined by the locus of the midcurve) and the cross-sectional orientation (defined by shear and torsion) of such structures in their deformed state, using distributed sensing of some kind. As mentioned in Ref. [1], distributed sensing may be grouped into two types: noncontact (the sensing mechanism is remote, such as using laser Doppler vibrometry (LDV)) and contact (the sensing mechanism is affixed to the object for in situ measurement). Like Ref. [1], this paper focuses on the latter group of sensing methods, since a large number of applications do not lend themselves to the strict limitations of noncontact methods, such as line-of-sight or ranging restrictions. Conventional contact sensors typically involve measurement of kinematic/kinetic properties such as strain or acceleration (distributed or discrete) and then obtain the global displaced shape by means of some inverse model. This paper further considers the case of the measurement of a finite set of local, uniaxial, discrete strain readings that are obtained through any type of sensing approach, including fiber Bragg grating (FBG), Rayleigh backscattering [13–15], or conventional resistive strain gauges. The aim is to develop a comprehensive inverse model that provides three-dimensional deformed shape and the kinematic generalized coordinates (like shear angles, curvatures, and elongations) from these limited set of uniaxial strain values. This paper extends the ideas presented in Ref. [1] and related works by including far

[1]Corresponding author.

Manuscript received September 27, 2016; final manuscript received January 16, 2017; published online February 9, 2017. Assoc. Editor: George Kardomateas.

more comprehensive mechanics in the model, allowing for applicability to a greater range of slender structures (such as non-negligible cross-sectional shear deformation). The remainder of this paper is presented as follows: Section 2 explains the kinematics of the approach, obtaining the uniaxial strain as a function of the deformation and geometric parameters (shear angles, curvatures, elongation, and the location of strain gauge), states the appropriate assumptions, and presents a locally exact solution basis on which to build a global deformed shape including the orientation of the cross section. Section 3 will present three cases of comparison of the exact analytical result (forward model simulation) compared to the predicted (inverse model) results. Finally, Sec. 4 will draw some observations, conclusions, and comparison with the results produced in Ref. [1].

2 Kinematic Model

2.1 Director Reference Frame in Generalized Coordinates. The initial shape of the structure may be curved or straight. We shall develop the theory of shape sensing based on the context of an initially straight configuration for simplicity. We assume that the initial shape (in which the strain gauges are attached in a zero-strain state to the structure) is known. Therefore, any subsequent strain measurements are referenced to this initial configuration. Thus, if the object is initially curved, we make a strain correction to the values of the strain obtained by gauges in the deformed state based on the theory developed further. The corrected strain values are the uniaxial strain in the deformed state of the object referring to the straight initial condition.

We begin by assuming that the initially straight object deforms to some current configuration. Consider a fixed orthogonal Cartesian triad $\mathbf{E} = \{\mathbf{E}_i\}$. Any configuration of the structure is defined by the locus of the centroid of the cross section called the midcurve defined by the position vector $\boldsymbol{\varphi}(\xi_1)$ parameterized by the undeformed arc-length $\xi_1 \in [0, L_0]$, where L_0 is the total length of the midcurve in the undeformed configuration, or

$$\boldsymbol{\varphi}(\xi_1) = \varphi_i(\xi_1)\mathbf{E}_i \tag{1}$$

The orientation of any cross section in the deformed configuration is quantified by the set of orthogonal Cosserat triad called directors $\{\mathbf{d}_i(\xi_1)\}$, such that

$$\mathbf{d}_i(\xi_1) = d_{ij}(\xi_1)\mathbf{E}_j \tag{2}$$

Assume the deformed arc-length coordinate is given by s. Consider that the object is subjected to purely axial strain. The infinitesimal length of the undeformed midcurve $d\xi_1$ deforms to ds such that the infinitesimal axial strain $e(\xi_1)$ is given by

$$e = \frac{ds - d\xi_1}{d\xi_1} \Rightarrow \frac{\partial \xi_1}{\partial s} = \frac{1}{1+e} \tag{3}$$

Assuming the position vector $\boldsymbol{\varphi}(\xi_1)$ to be differentiable in ξ_1, we may exploit the differential geometry of the midcurve to evaluate the tangent vector $\mathbf{T}(\xi_1)$ in terms of the pitch angle $\theta(\xi_1)$ and yaw angle $\phi(\xi_1)$ and as the derivative of the position vector using Eq. (3)

$$\begin{aligned}\mathbf{T}(\xi_1) &= \cos\theta(\xi_1)\cos\phi(\xi_1)\mathbf{E}_1 + \sin\theta(\xi_1)\mathbf{E}_2 \\ &\quad + \cos\theta(\xi_1)\sin\phi(\xi_1)\mathbf{E}_3 \\ \frac{\partial \boldsymbol{\varphi}(\xi_1)}{\partial s} &= \frac{\partial \boldsymbol{\varphi}(\xi_1)}{\partial \xi_1}\frac{\partial \xi_1}{\partial s} = \frac{1}{1+e}\frac{\partial \boldsymbol{\varphi}(\xi_1)}{\partial \xi_1} = \mathbf{T}(\xi_1)\end{aligned} \tag{4}$$

Therefore, the position vector to the centerline midcurve may be written in terms of two angles and the axial strain as

$$\begin{aligned}\boldsymbol{\varphi} &= \left(\int_0^{\xi_1} (\cos\theta\cos\phi)(1+e)d\xi_1\right)\mathbf{E}_1 \\ &\quad + \left(\int_0^{\xi_1} \sin\theta(1+e)d\xi_1\right)\mathbf{E}_2 \\ &\quad + \left(\int_0^{\xi_1} \cos\theta\sin\phi(1+e)d\xi_1\right)\mathbf{E}_3\end{aligned} \tag{5}$$

The position vector $\boldsymbol{\varphi}(\xi_1)$ defines the midcurve but not the orientation of the cross section that is affected by means of shear and torsion. The directors take care of this. Assume a cross section that does not experience shear and torsion. Another triad $\mathbf{P} = \{\mathbf{T}(\xi_1), \mathbf{V}(\xi_1), \mathbf{H}(\xi_1)\}$ is defined. It originates at the centroid of each cross section such that the vectors $\mathbf{T}(\xi_1)$ and $\mathbf{V}(\xi_1)$ lie in the pitch angle plane, and thus, $\mathbf{H}(\xi_1) = \mathbf{T}(\xi_1) \times \mathbf{V}(\xi_1)$. Thus,

$$\begin{bmatrix}\mathbf{T}(\xi_1)\\ \mathbf{V}(\xi_1)\\ \mathbf{H}(\xi_1)\end{bmatrix} = \begin{bmatrix}\cos\theta\cos\phi & \sin\theta & \cos\theta\sin\phi\\ -\sin\theta\cos\phi & \cos\theta & -\sin\theta\sin\phi\\ -\sin\phi & 0 & \cos\phi\end{bmatrix}\begin{bmatrix}\mathbf{E}_1\\ \mathbf{E}_2\\ \mathbf{E}_3\end{bmatrix}, \quad \mathbf{P} = \mathbf{W}_1\mathbf{E} \tag{6}$$

If the object is subjected to shear and torsion, the orientation of the cross section changes. The tangent vector is no longer perpendicular to the cross section. The shearing effect can be quantified by three shear angles $\gamma_{11}(\xi_1)$, $\pi/2 - \gamma_{12}(\xi_1)$, and $\pi/2 - \gamma_{13}(\xi_1)$ subtended by the directors $\mathbf{d}_1(\xi_1)$, $\mathbf{d}_2(\xi_1)$, and $\mathbf{d}_3(\xi_1)$ with the tangent vector $\mathbf{T}(\xi_1)$, respectively. The directors $\mathbf{d}_2(\xi_1)$ and $\mathbf{d}_3(\xi_1)$ span the cross section. Therefore, any point in the structure is given by the position vector

$$\mathbf{R}(\xi_1) = \boldsymbol{\varphi}(\xi_1) + \xi_2\mathbf{d}_2(\xi_1) + \xi_3\mathbf{d}_3(\xi_1) \tag{7}$$

Note that any point in the object in undeformed state is quantified by the material points $\{\xi_1, \xi_2, \xi_3\}$. If the point p represents the point of intersection of the cross section with the midcurve, and q being any point on the object, since the cross section is rigid, point q can always be positioned by the position vector $\mathbf{r}_{pq} = \xi_2\mathbf{d}_2(\xi_1) + \xi_3\mathbf{d}_3(\xi_1)$. Figure 1 shows the geometry of the deformed structure and the related parameters. To establish a relationship between $\mathbf{P} = \{\mathbf{T}(\xi_1), \mathbf{V}(\xi_1), \mathbf{H}(\xi_1)\}$ and $\mathbf{D} = \{\mathbf{d}_1(\xi_1), \mathbf{d}_2(\xi_1), \mathbf{d}_3(\xi_1)\}$, it is necessary to define three angles $\alpha_1(\xi_1)$, $\alpha_2(\xi_1)$, and $\alpha_3(\xi_1)$ subtended by the directors $\mathbf{d}_1(\xi_1)$, $\mathbf{d}_2(\xi_1)$, and $\mathbf{d}_3(\xi_1)$ with the vector $\mathbf{V}(\xi_1)$, respectively, as shown in Fig. 1.

Therefore,

$$\begin{aligned}\mathbf{T} &= \cos(\gamma_{11}(\xi_1))\mathbf{d}_1 + \sin(\gamma_{12}(\xi_1))\mathbf{d}_2 + \sin(\gamma_{13}(\xi_1))\mathbf{d}_3\\ \mathbf{V} &= \cos(\alpha_1(\xi_1))\mathbf{d}_1 + \cos(\alpha_2(\xi_1))\mathbf{d}_2 + \cos(\alpha_3(\xi_1))\mathbf{d}_3\\ \mathbf{H} &= \mathbf{T}\times\mathbf{V}\\ \begin{bmatrix}\mathbf{T}(\xi_1)\\ \mathbf{V}(\xi_1)\\ \mathbf{H}(\xi_1)\end{bmatrix} &= \mathbf{W}_2\begin{bmatrix}\mathbf{d}_1\\ \mathbf{d}_2\\ \mathbf{d}_3\end{bmatrix} \Rightarrow \mathbf{P} = \mathbf{W}_2\mathbf{D}\end{aligned} \tag{8}$$

For the transformation $\mathbf{W}_2$ to be orthonormal, the parameters α_i and γ_{1i}, where $i = 1, \ldots, 3$, must be such that $\mathbf{T}(\xi_1)$, $\mathbf{V}(\xi_1)$, and $\mathbf{H}(\xi_1)$ are orthonormal. These would result in six constraint equations, three for the orthonormal conditions and the other three for

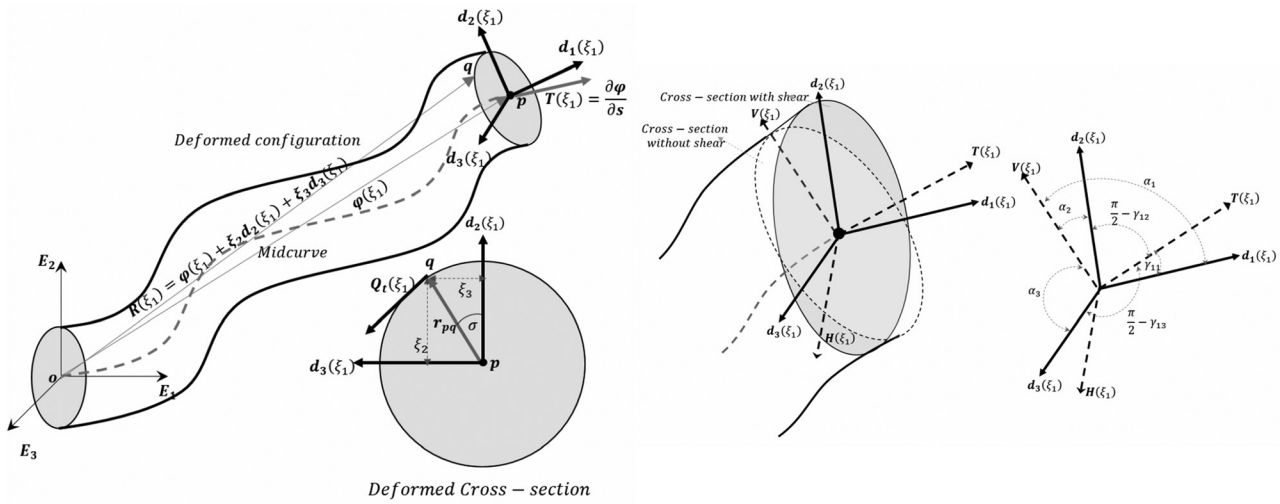

Fig. 1 Deformed configuration of the beam and material-adapted frame (left) and relationship between {d_1, d_2, d_3} and {T, V, H} material frame of reference (right)

vanishing the derivatives of the magnitude of the vectors $\mathbf{T}(\xi_1)$, $\mathbf{V}(\xi_1)$, and $\mathbf{H}(\xi_1)$. Equations (6) and (8) establish a relationship between the triad $\mathbf{D} = \{\mathbf{d}_1(\xi_1), \mathbf{d}_2(\xi_1), \mathbf{d}_3(\xi_1)\}$ and $\mathbf{E} = \{\mathbf{E}_1, \mathbf{E}_2, \mathbf{E}_3\}$

$$\mathbf{D} = \mathbf{W}_2^{-1}\mathbf{W}_1\mathbf{E} = \mathbf{Y}(\xi_1)\mathbf{E} \tag{9}$$

The derivative of the directors may be obtained from Eq. (9). It is observed that the derivatives of directors $\mathbf{D}'$ are related to the director triad $\mathbf{D}$ by means of an antisymmetric curvature matrix, as expected, because the directors are orthonormal and the change in directors consists of rotation alone. Thus,

$$\mathbf{D}' = (\mathbf{W}_2^{-1}\mathbf{W}_1)'\mathbf{E} = (\mathbf{W}_2^{-1}\mathbf{W}_1)'.(\mathbf{W}_2^{-1}\mathbf{W}_1)^{-1}\mathbf{D} = \mathbf{Y}'\mathbf{Y}^{-1}\mathbf{D} = \mathbf{K}.\mathbf{D}$$
$$\mathbf{K} = \begin{bmatrix} 0 & \bar{\kappa}_3 & -\bar{\kappa}_2 \\ -\bar{\kappa}_3 & 0 & \bar{\kappa}_1 \\ \bar{\kappa}_2 & -\bar{\kappa}_1 & 0 \end{bmatrix} = \mathbf{Y}'\mathbf{Y}^{-1} \tag{10}$$

The derivative of any director may be considered as a tensor operation such that

$$\frac{\partial \mathbf{d}_i(\xi_1)}{\partial \xi_1} = \boldsymbol{\psi}\mathbf{d}_i = \boldsymbol{\kappa} \times \mathbf{d}_i \tag{11}$$

The tensor $\boldsymbol{\psi}$ is the curvature tensor and being antisymmetric in nature, it has a uniaxial Darboux vector $\boldsymbol{\kappa} = \bar{\kappa}_1\mathbf{d}_1 + \bar{\kappa}_2\mathbf{d}_2 + \bar{\kappa}_3\mathbf{d}_3$ associated with it. The components of the curvature matrix in terms of the generalized coordinates defined above can be found using Eq. (10) and are defined in the Appendix. From Eqs. (4), (8), and (10), the following relationship can be written:

$$\begin{bmatrix} \boldsymbol{\varphi}' \\ \mathbf{d}_1' \\ \mathbf{d}_2' \\ \mathbf{d}_3' \end{bmatrix} = \begin{bmatrix} 0 & (1+e)\cos\gamma_{11} & (1+e)\sin\gamma_{12} & (1+e)\sin\gamma_{13} \\ 0 & 0 & \bar{\kappa}_3 & -\bar{\kappa}_2 \\ 0 & -\bar{\kappa}_3 & 0 & \bar{\kappa}_1 \\ 0 & \bar{\kappa}_2 & -\bar{\kappa}_1 & 0 \end{bmatrix} \begin{bmatrix} \boldsymbol{\varphi} \\ \mathbf{d}_1 \\ \mathbf{d}_2 \\ \mathbf{d}_3 \end{bmatrix} \tag{12}$$

The above equation expresses the derivatives of the directors and the position vectors in terms of the kinematic parameters of deformation and their derivatives. Note that the explicit dependence on ξ_1 is omitted for brevity. Given this material-adapted geometry, we shall evaluate the uniaxial strain in Sec. 2.2.

It is worth mentioning that if there is no shear and the axial extension is zero, then the problem reduces to that solved in Ref. [1]. These assumptions would imply $\gamma_{1i}(\xi_1) = 0, \alpha_1(\xi_1) = \pi/2, \alpha_2(\xi_1) = 0$, $\alpha_3(\xi_1) = \pi/2$, and $e(\xi_1) = 0$, respectively, where $i = 1, \ldots, 3$. This would also imply $\mathbf{d}_1(\xi_1) = \mathbf{T}(\xi_1)$, $\mathbf{d}_2(\xi_1) = \mathbf{V}(\xi_1)$, and $\mathbf{d}_3(\xi_1) = \mathbf{H}(\xi_1)$. Making all these substitutions will lead to Eq. (5) in Ref. [1]. Therefore, the current relationship consistently reduces to the simpler one described in Ref. [1].

2.2 Strain. The most generalized approach to find the strain vector is to compute the derivative of the position vector of any point in the object subtracted by the director $\mathbf{d}_1$. This is because the magnitude of the first component of any vector in the undeformed state is changed, whereas the magnitude of the second and third component remains the same due to the assumption of the cross section being rigid. The total change in the first component is comprised of the vector elongation and rotation. Subtraction of $\mathbf{d}_1$ removes the rotation effect from the net change given by the derivative of the position vector. The strain vector can also be obtained from the deformation gradient tensor as in Ref. [16]. From Fig. 1 and Eq. (7), the strain vector at any point in the structure is given by

$$\begin{aligned} \boldsymbol{\epsilon} &= \frac{\partial \mathbf{R}}{\partial \xi_1} - \mathbf{d}_1 \\ &= \frac{\partial}{\partial \xi_1}(\boldsymbol{\varphi} + \xi_2\mathbf{d}_2 + \xi_3\mathbf{d}_3) - \mathbf{d}_1 = \boldsymbol{\varphi}_{,\xi_1} + \xi_2\mathbf{d}_{2,\xi_1} + \xi_3\mathbf{d}_{3,\xi_1} - \mathbf{d}_1 \end{aligned} \tag{13}$$

From Eqs. (12) and (13), the strain vector can be written as

$$\begin{aligned} \boldsymbol{\epsilon} = &\{((1+e)\cos\gamma_{11} - 1) - \xi_2\bar{\kappa}_3 + \bar{\kappa}_2\xi_3\}\mathbf{d}_1 \\ &+ \{(1+e)\sin\gamma_{12} - \bar{\kappa}_1\xi_3\}\mathbf{d}_2 + \{(1+e)\sin\gamma_{13} + \bar{\kappa}_1\xi_2\}\mathbf{d}_3 \end{aligned} \tag{14}$$

Consider a typical point q on the surface of the deformed structure as shown in Fig. 1. The vector $\mathbf{r}_{pq}$ makes an angle σ with the vector $\mathbf{d}_2$. If the magnitude of relative position vector $\mathbf{r}_{pq}$ is taken as $r = \xi_2^2 + \xi_3^2$, then the material points ξ_2 and ξ_3 can be written

as $r\cos\sigma$ and $r\sin\sigma$, respectively. The vector $\mathbf{Q}_t$ in Fig. 1 can be easily obtained as $-\sin\sigma\mathbf{d}_2+\cos\sigma\mathbf{d}_3$, which is the cross-product of the director $\mathbf{d}_1$ and the unit vector in the direction of $\mathbf{r}_{pq}$.

Assume a strain gauge is placed on the surface of the object at point q oriented in some arbitrary direction spanning the $(\mathbf{d}_1,\mathbf{Q}_t)$ plane, i.e., $\cos\mu\mathbf{d}_1+\sin\mu\mathbf{Q}_t$. When $\mu=0$, the inclination of the strain gauge coincides with the director $\mathbf{d}_1$. The scalar strain ε experienced by that gauge would be Eq. (14) along this direction. Therefore, ε is the dot product of Eq. (14) with the direction vector $\cos\mu\mathbf{d}_1+\sin\mu\mathbf{Q}_t$. Before obtaining the scalar strain, we make the following definitions of the strain terms that will further simplify Eq. (14):

$$\begin{aligned} S_1&=((1+e)\cos\gamma_{11}-1)\\ S_2&=(1+e)\sin\gamma_{12}\\ S_3&=(1+e)\sin\gamma_{13}\\ S_4&=r\bar{\kappa}_1,\ \ S_5=r\bar{\kappa}_2,\ \ S_6=r\bar{\kappa}_3 \end{aligned} \tag{15}$$

Using Eqs. (14) and (15), along with the definition of ξ_2 and ξ_3, the scalar strain is thus given by

$$\begin{aligned}\varepsilon=&\{S_1-S_6\cos\sigma+S_5\sin\sigma\}\cos\mu-\{S_2-S_4\sin\sigma\}\sin\mu\sin\sigma\\&+\{S_3+S_4\cos\sigma\}\sin\mu\cos\sigma\end{aligned} \tag{16}$$

2.3 Solution Approach. It is clear from Eqs. (15) and (16) that in order to determine all the deformation parameters $\{e,\gamma_{11},\gamma_{12},\gamma_{13},\bar{\kappa}_1,\bar{\kappa}_2,\bar{\kappa}_3\}$, a minimum of six values of scalar strains (or strain gauges) are required per cross section. It is an inverse problem going from Eq. (16) back to $\boldsymbol{\varphi},\mathbf{d}_1,\mathbf{d}_2$, and $\mathbf{d}_3$ via Eq. (12). To obtain the approximate solution, the structure is discretized into N segments $(n=1,\ldots,N)$ with the center of each segment located at $\bar{\xi}_{1n}$. As in Ref. [1], a finite set of discrete strain measurements are available along the object at various $\xi_1=\xi_{1n}$ at angles σ_m $(m=1,\ldots,6)$ for each given location ξ_{1n} along the centerline. Thus, the scalar strain at the nth cross section and the mth strain gauge is given by

$$\begin{aligned}\varepsilon_{n,m}=&\{S_{1_n}-S_{6_n}\cos\sigma_{n,m}+S_{5_n}\sin\sigma_{n,m}\}\cos\mu_{n,m}\\&-\{S_{2_n}-S_{4_n}\sin\sigma_{n,m}\}\sin\mu_{n,m}\sin\sigma_{n,m}\\&+\{S_{3_n}+S_{4_n}\cos\sigma_{n,m}\}\sin\mu_{n,m}\cos\sigma_{n,m}\end{aligned} \tag{17}$$

where $\sigma_{n,m}$ is the angle σ subtended by the mth strain gauge on the surface of nth cross section, and $\mu_{n,m}$ is the angle μ subtended by the mth strain gauge on the surface of nth cross section.

Equation (17) is a linear system relating strain (ε) to the deformation parameters $(S_i$, where $i=1,\ldots,6)$ and is invertible to give the strain measures in terms of strains. For the nth cross section, the discretized form of Eq. (12) becomes

$$\begin{bmatrix}\boldsymbol{\varphi}_n'\\ \mathbf{d}_{1_n}'\\ \mathbf{d}_{2_n}'\\ \mathbf{d}_{3_n}'\end{bmatrix}=\begin{bmatrix}0 & S_{1_n}+1 & S_{2_n} & S_{3_n}\\ 0 & 0 & \frac{S_{6_n}}{r} & -\frac{S_{5_n}}{r}\\ 0 & -\frac{S_{6_n}}{r} & 0 & \frac{S_{4_n}}{r}\\ 0 & \frac{S_{5_n}}{r} & -\frac{S_{4_n}}{r} & 0\end{bmatrix}\begin{bmatrix}\boldsymbol{\varphi}_n\\ \mathbf{d}_{1_n}\\ \mathbf{d}_{2_n}\\ \mathbf{d}_{3_n}\end{bmatrix} \tag{18}$$

Ignoring the first row relating the position vector $\boldsymbol{\varphi}_n$ with the directors $\{\mathbf{d}_{1_n},\mathbf{d}_{2_n},\mathbf{d}_{3_n}\}$ and the first column, the next three lines of Eq. (18) represent a linear antisymmetric first-order simultaneous differential equations with coefficients S_i, where $i=1,\ldots,6$. We use a local linearization approach, linearizing the coefficients in Eq. (18) locally in each nth segment and solve analytically. We truncate a Taylor series expansion of the six coefficients about $\xi_1=\xi_{1_n}$ in each segment to zeroth order, such that $\xi_1\approx\xi_{1_n}$. This converts Eq. (18) into a constant-coefficient system that admits exact solutions, valid locally at each cross section n. Since the frame is body centric, there is no singularity provided the angles $\sigma_{n,m}$ and $\mu_{n,m}$ are such that Eq. (17) is solvable, the solution to the locally linearized version of Eq. (18) for $\boldsymbol{\varphi}_n$ is

$$\begin{aligned}&\boldsymbol{\varphi}_n(\xi_1)\\&=\sum_{i=1}^{3}\mathbf{C}_{n,i}\left(a_{ni1}+a_{ni2}\sin\left(\frac{\xi_1\gamma_n}{r}\right)+a_{ni3}\cos\left(\frac{\xi_1\gamma_n}{r}\right)\right)+\mathbf{C}_{n,4}\end{aligned}$$

or

$$\begin{aligned}\boldsymbol{\varphi}_n(\xi_1)=&\mathbf{A}_{n,1}+\mathbf{A}_{n,2}\sin\left(\frac{\xi_1\gamma_n}{r}\right)\\&+\mathbf{A}_{n,3}\cos\left(\frac{\xi_1\gamma_n}{r}\right),\ \ \text{where}\ \gamma_n=\left(\sum_{i=4}^{6}S_{i_n}^2\right)^{\frac{1}{2}}\end{aligned} \tag{19}$$

The localized linear solution of the position vector $\boldsymbol{\varphi}_n(\xi_1)$ contains four vector integration constants $\mathbf{C}_{n,j}$, $j=1,\ldots,4$. The parameters $a_{n_{ij}}$ and the vector $\mathbf{A}_{n,i}$ are functions of $(r,\ \xi_1,\ S_{m_n})$ and $(r,\ \xi_1,\ S_{m_n},\mathbf{C}_{n,j})$, respectively, where $m=1\ldots6,i,j=1\ldots3$. These parameters are defined in the Appendix. The solutions to the directors $\{\mathbf{d}_{i_n}(\xi_1)\}$ bear the same form as Eq. (18) except with different vector constants. Thus, if there are N cross sections, there are $12N$ constants to be determined. Imposing continuity in each component of $\{\boldsymbol{\varphi}_n(\xi_1),\mathbf{d}_{1_n}(\xi_1),\mathbf{d}_{2_n}(\xi_1),\mathbf{d}_{3_n}(\xi_1)\}$ between segments, e.g., halfway between ξ_{1_n} and $\xi_{1_{n+1}}$, gives $11N$ constraints, and the remaining N constraints may be obtained by imposing an appropriate boundary condition.

With the constraints imposed, Eq. (19) represents a locally exact basis by which the measured strains may be related back to the global displacement. It is important to note that if all the measured strains are zero, i.e., $S_{i_n}=0,\ \ i=1\ldots6$, then

$$\begin{aligned}\lim_{S_{i_n}\to0}\boldsymbol{\varphi}_n(\xi_1)&=\mathbf{C}_{n,1}\xi_1+\mathbf{C}_{n,4}\\ \lim_{S_i\to0}\mathbf{d}_{i_n}(\xi_1)&=\mathbf{C}_{n,i},\ \ \text{where}\ \ i=1,\ldots,3\end{aligned} \tag{20}$$

Thus, the solution basis has no singularities like the Frenet frame or others may have. In practice, then, for each segment n, either Eq. (19) or (20) may be used as the local solution basis, depending on whether all of the six measured strain quantities are within some user-specified tolerance value. Thus, the global displacement is explicitly expressed as a function of measured strains. The global displacement of the structure and the directors may then be constructed using Eq. (21) in Ref. [1]. The axial strain and shear angles at the nth cross section can be easily obtained from Eq. (15). The pitch and yaw angles at the cross sections bearing strain gauges may be obtained by equating the component of the tangent vector in Eqs. (6) and (8), after substituting the components of the directors as obtained by solving Eq. (19).

The result of the directors obtained from Eq. (18) is in agreement with the Rodrigues formula of rotation [17]. The interpretation of the directors $\mathbf{d}_{i_n}$ using the Rodrigues formula provides great insight toward the solution obtained from Eq. (18). The Darboux vector, $\boldsymbol{\kappa}$, may be interpreted as the rotation of the director frame per unit arc-length at ξ_1 by an angle $\|\boldsymbol{\kappa}\|=\sqrt{\bar{\kappa}_1^2+\bar{\kappa}_2^2+\bar{\kappa}_3^2}$. For the discretized cross section at ξ_{1_n}, the curvature terms are constant as defined in Eq. (15). It is clear from Eq. (15) that $\|\boldsymbol{\kappa}_n\|=(\gamma_n/r)$. Therefore, the director $\mathbf{d}_{i_n}(\xi_{1_n})$ is obtained by rotating the director $\mathbf{d}_i(0)=\mathbf{E}_i$ by an angle $\int_0^{\xi_1}\|\boldsymbol{\kappa}_n\|d\xi_1=(\xi_1\gamma_n/r)$

about the unit vector $\boldsymbol{\eta}_n$. Let $\Re_n$ be the antisymmetric matrix corresponding to the axial vector $\boldsymbol{\eta}_n$ such that for any vector $\mathbf{v}$, $\Re_n\mathbf{v} = \boldsymbol{\eta}_n \times \mathbf{v}$, and $\Re_n^2\mathbf{v} = \boldsymbol{\eta}_n \times (\boldsymbol{\eta}_n \times \mathbf{v})$. Hence from Rodrigues formula

$$\begin{aligned}\mathbf{d}_{i_n}(\xi_1) &= \left[\mathbf{d}_i(0) + \boldsymbol{\eta}_n \times \left(\boldsymbol{\eta}_n \times \mathbf{d}_i(0)\right)\right] + \left(\boldsymbol{\eta}_n \times \mathbf{d}_i(0)\right)\sin\left(\frac{\xi_1\gamma_n}{r}\right) \\ &\quad - \left[\boldsymbol{\eta}_n \times \left(\boldsymbol{\eta}_n \times \mathbf{d}_i(0)\right)\right]\cos\left(\frac{\xi_1\gamma_n}{r}\right) = \boldsymbol{\psi}_n\mathbf{d}_i(0) \\ &= e^{\left(\frac{\xi_1\gamma_n}{r}\right)\Re_n}\mathbf{d}_i(0)\end{aligned} \tag{21}$$

where

$$\boldsymbol{\eta}_n = \frac{\boldsymbol{\kappa}\left(\xi_{1_n}\right)}{\|\boldsymbol{\kappa}_n\|} = \frac{S_{4_n}}{\gamma_n}\mathbf{d}_{1_n} + \frac{S_{5_n}}{\gamma_n}\mathbf{d}_{2_n} + \frac{S_{6_n}}{\gamma_n}\mathbf{d}_{3_n}$$

and

$$\boldsymbol{\psi}_n = \mathbf{I}_3 + \sin\left(\frac{\xi_1\gamma_n}{r}\right)\Re_n + \left(1 - \cos\left(\frac{\xi_1\gamma_n}{r}\right)\right)\Re_n^2$$

The shape sensing algorithm developed above by assuming terms in Eq. (18) to be constants (obtained by strain measurements) gives the directors at cross section at ξ_{1_n} by imposing continuity between the segments. This explains the improvement of results if the object is divided into large number of segments. The directors $\mathbf{d}_{i_n}(\xi_1)$ at any arbitrary ξ_1 in the segment n is then predicted by the shape functions given by Eq. (21) in Ref. [1].

3 Results and Discussion

Three different three-dimensional shapes of varying complexity in deformation/strain patterns were simulated. In order to investigate the ability of Eqs. (15) and (19) to predict the global displacement from locally measured strain, a long rod with a length 300 m (984.252 ft) and diameter of 30 cm (12 in.) was simulated. It is noteworthy that the simulations are independent of material properties because inverse shape sensing requires only the kinematic and geometric parameters that define the displacement and strains. The strain value at the surface for the given deformed shape at set cross sections for the given directions of strain gauges was obtained analytically using Eq. (16). From the values of the strain parameters $\{S_{1_n}, S_{2_n}, S_{3_n}, S_{4_n}, S_{5_n}, S_{6_n}\}$, Eqs. (15) and (19) were used to reconstruct the shape and obtain directors. For all the three simulations, fixed set angles $\sigma_n = \{\pi/4, \pi/2, 3\pi/4, \pi, 5\pi/4, 3\pi/2\}$ and $\mu_n = \{\pi/4, -\pi/4, \pi/4, -\pi/4, \pi/4, -\pi/4\}$ are assumed. This selection is done so that Eq. (17) is invertible. Different studies are carried for the three simulations, and the results are discussed.

3.1 Simulation 1. The first simulation has a shape similar to simulation 1 in Ref. [1], except that it is 300 m long. This simulation studies the effect of curvature and constantly increasing torsion from the fixed end toward the distal end ($0 - 0.75\ \pi$ rad). Bearing long length (300 m) as compared to the simulation in Ref. [1] (212 m) and presence of additional torsion make this simulation more complicated than the one in Ref. [1]. The simulation was run for six (three of them are showed in Fig. 2) different cases varying the number of equally spaced strain values to simulate different sensor counts. It is important to note that six sensors are required for each cross section, which implies a total of $6N$ sensors, where N indicates the number of cross section along the

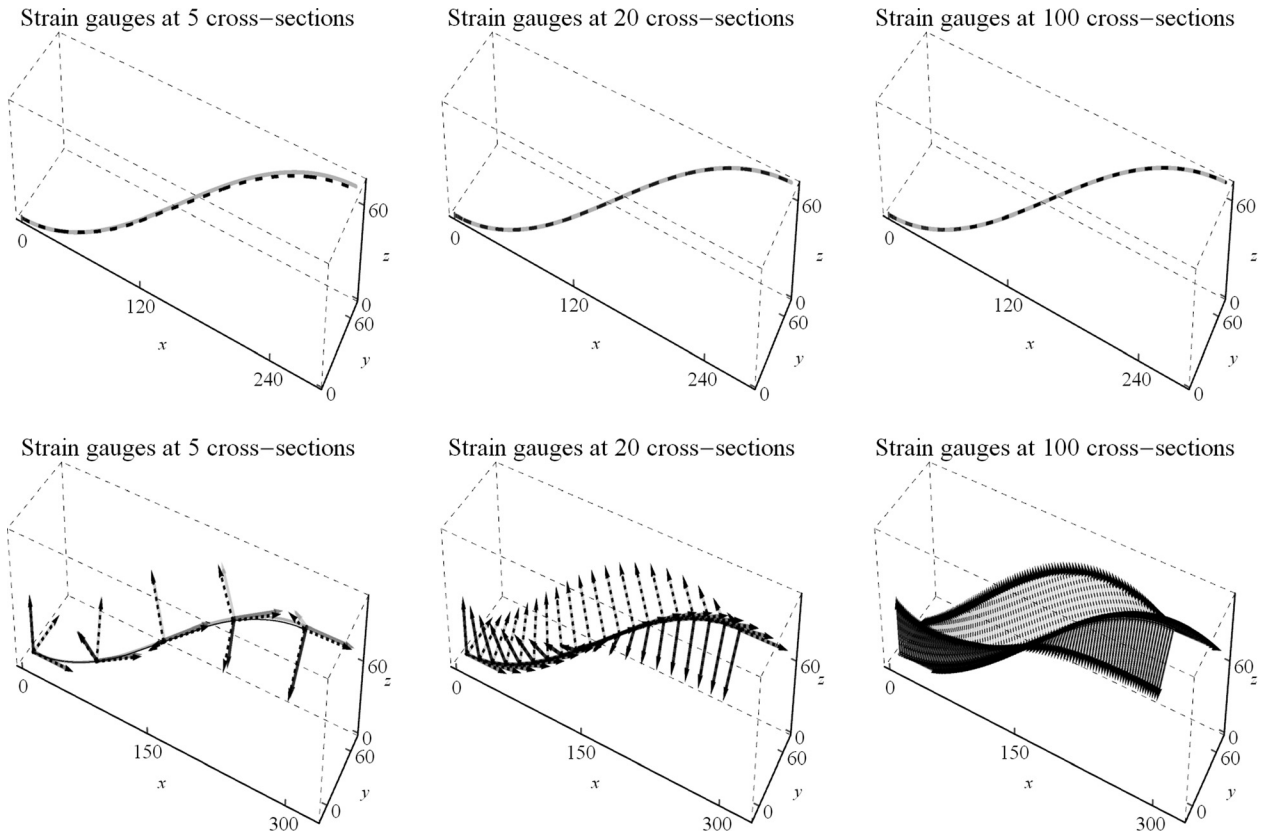

Fig. 2 Comparison of simulation 1 centerlines of exact (light-gray solid line) and reconstructed via strain (dashed lines) (top plots) and exact directors ($\mathbf{d}_1$, $\mathbf{d}_2$, and $\mathbf{d}_3$ are represented by solid medium, light, and dark gray vectors, respectively) and the predicted directors (black-dashed directors) (bottom plots) of the object

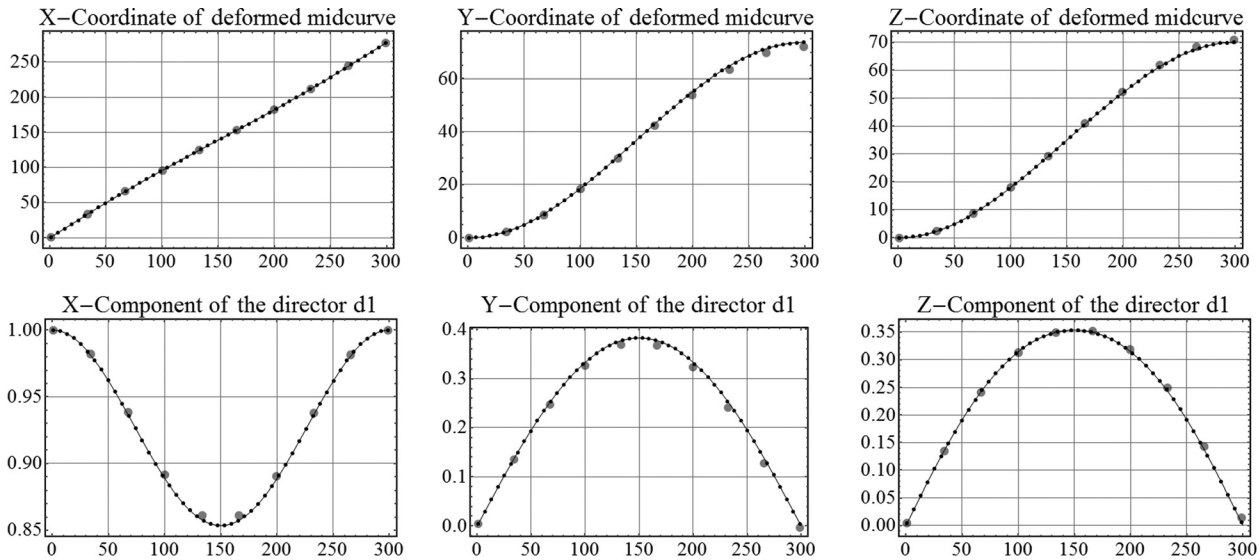

Fig. 3 Comparison of simulation 1 exact (black line) position vector components (top plots) and director $\mathbf{d}_1$ components (bottom plots) with the predicted components for ten strain gauge locations (gray dots) and 50 strain gauge locations (black dots), where *x*-axis represents ξ_1

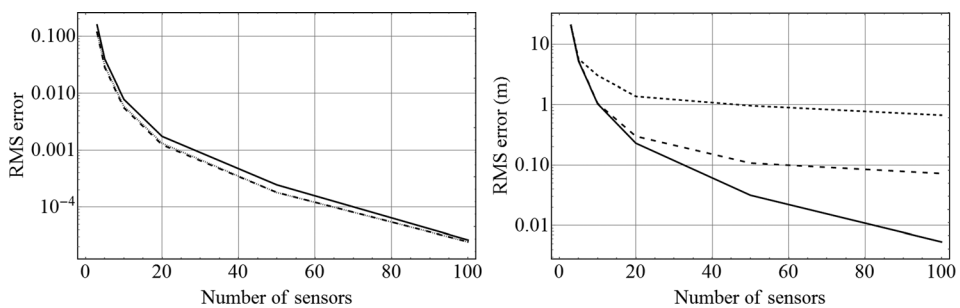

Fig. 4 Left plot showing root mean square error for the directors—$\mathbf{d}_1$ (solid line), $\mathbf{d}_2$ (dashed line), and $\mathbf{d}_3$ (dotted line) for no noise case and the right plot showing the rms error for the position vector for various noise level—no noise (solid line), [−5,5] microstrain uniform noise (dashed line), and [−50,50] microstrain uniform noise (dotted line)

length where these sensors are placed. For simulation 1, $N = 3,\ 5,\ 10,\ 20,\ 50$, and 100 (18, 30, 60, 120, and 600 total sensors, respectively) are considered. The distal end was displaced almost by 70 m in both *y*- and *z*-directions from the initially straight configuration.

Figure 2 compares the exact (imposed) centerline (light-gray solid curve) with the reconstructed centerline and the exact cross-sectional orientation ($\mathbf{d}_1$, $\mathbf{d}_2$, and $\mathbf{d}_3$ are represented by solid medium, light, and dark gray vectors, respectively) with the predicted directors (dashed black vectors), solved using the linearized analytical inverse approach (Eqs. (15) and (19)) for simulation 1 for $N = 5, 20$, and 100. For as few as five and ten cross sections (spaced approximately 60 m and 30 m, respectively), excellent reconstruction is observed with an average (over the full length) root mean square error of only 5.2 m and 1.03 m, respectively. Secondly for ten cross sections, the rms error for the directors $\mathbf{d}_1$, $\mathbf{d}_2$, and $\mathbf{d}_3$ is merely 0.0078, 0.0056, and 0.0059, respectively, thus predicting the cross-sectional orientation efficiently. If the same simulation is run for the length of cable as 212 m and no torsion for five sensor locations (exactly as in Ref. [1]), the error comes out to be the same (1.1 m) as obtained by the formulation presented in Ref. [1]. This clearly reflects the fact that the formulation presented in this paper is a general form that can capture many more mechanical effects as compared to the formulation in Ref. [1], which could capture only curvature changes. Increment of number of sensor locations improves the shape reconstruction, thereby reducing the rms error to as low as 3 mm for 50 sensor locations (one every 6 m).

Figure 3 represents the comparison of the exact component of $(\boldsymbol{\varphi}, \mathbf{d}_1)$ represented by a solid black line with the components predicted by ten strain measurement locations (large gray dots) and 50 strain measurement locations (black dots). The figure shows good convergence with the increase of the number of sensors. Since the object in simulation 1 is not deformed in a very complicated shape, ten sensor locations do a good reconstructing of the shape.

All these results presented above are for the ideal case of perfect strain transfer from the structure to the attached strain gauges with certainty in the assumed boundary conditions and no other external noise influence on the system (environmental or numerical). As in Ref. [1], to examine these influences for a first-order assessment of robustness, uniformly distributed random noise was added to the strain values, at a [−5,5] microstrain level (representative of the most conventional strain gauge systems) and at [−50,50] microstrain level (severe noise) before being input into the reconstruction algorithm. Fifty such realizations were performed in a Monte Carlo sense, and the average rms error was computed for different number of sensor counts at each noise level. It is observed that at each sensor count, the noise increases the error with gradual improvement as the sensor count increases.

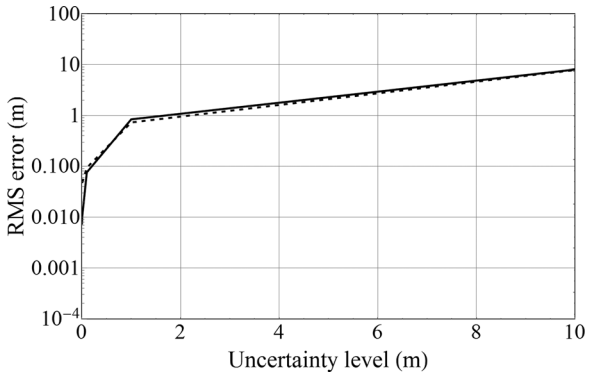

Fig. 5 Average root mean square error in the shape reconstruction for simulation 1 (solid line) and simulation 2 (dashed line) as a function of the uncertainty level in the initial displacement conditions at the proximal end

Figure 4 (right plot) gives the rms error in the position vector for different noise level, and the left plot represents the rms error plot for the directors.

Figure 5 shows the effect of the uncertainty on the specifications of the boundary condition at the proximal end ($\xi_1 = 0$), using 100 sensors by choosing 50 random boundary conditions at proximal end over [−0.0001, 0.0001] m, [−0.01,0.01] m, [−0.1,0.1] m, [−1,1] m, and [−10,10] m and obtaining the average rms value (averaged over 50 simulation) for both the simulations. It is clear that with the new approach, the trend still remains linear as in Ref. [1], with the averaged rms error being proportional to the input boundary condition uncertainty level.

3.2 Simulation 2. In simulation 2, the object with same geometric and kinematic configuration as in simulation 1 is subjected to torsion, nonuniform elongation, shear, and complex curvature changes, making it more general. This is where the power of this method becomes evident. If L_0 represents the total undeformed arc-length, then the imposed axial strain and the shear angles are given in the below equation

$$e(\xi_1) = \frac{20\pi}{L_0}\cos\left(\frac{\pi\xi_1}{2L_0}\right)$$
$$\gamma_{11} = \frac{\pi\xi_1}{16L_0}; \quad \gamma_{12} = \frac{\pi\xi_1}{32L_0} \tag{22}$$
$$\alpha_3 = \frac{\pi}{2}\left(1 + \frac{0.2\xi_1}{L_0}\right)$$

It must be noted that the angles γ_{13}, α_1, and α_2 may be obtained using the constraints in generalized coordinates γ_{1i} and α_i, where $i = 1, \ldots, 3$, as mentioned immediately after Eq. (8). The displacement of the distal end is about 193 m and 116 m in the y- and z-directions. Since the shape and deformation are complicated, the study is performed for a minimum of ten sensor locations (with $N = 10$, 20, 50, and 100) unlike a minimum of three sensor locations in simulation 1. The rms error for the position vector decreases from 9.8 m using ten sensor locations to 4.8 cm with 100 sensor locations, representing excellent convergent reconstruction.

The top three plots in Fig. 6 compare the exact (imposed) centerline (gray curve) with the reconstructed centerline for the second simulation and the bottom three plots compares the exact cross-sectional orientation ($\mathbf{d}_1$, $\mathbf{d}_2$, and $\mathbf{d}_3$ are represented by solid medium, light, and dark gray vectors, respectively) with the predicted directors for $N = 10$, 20, and 100. Figure 7 represents the

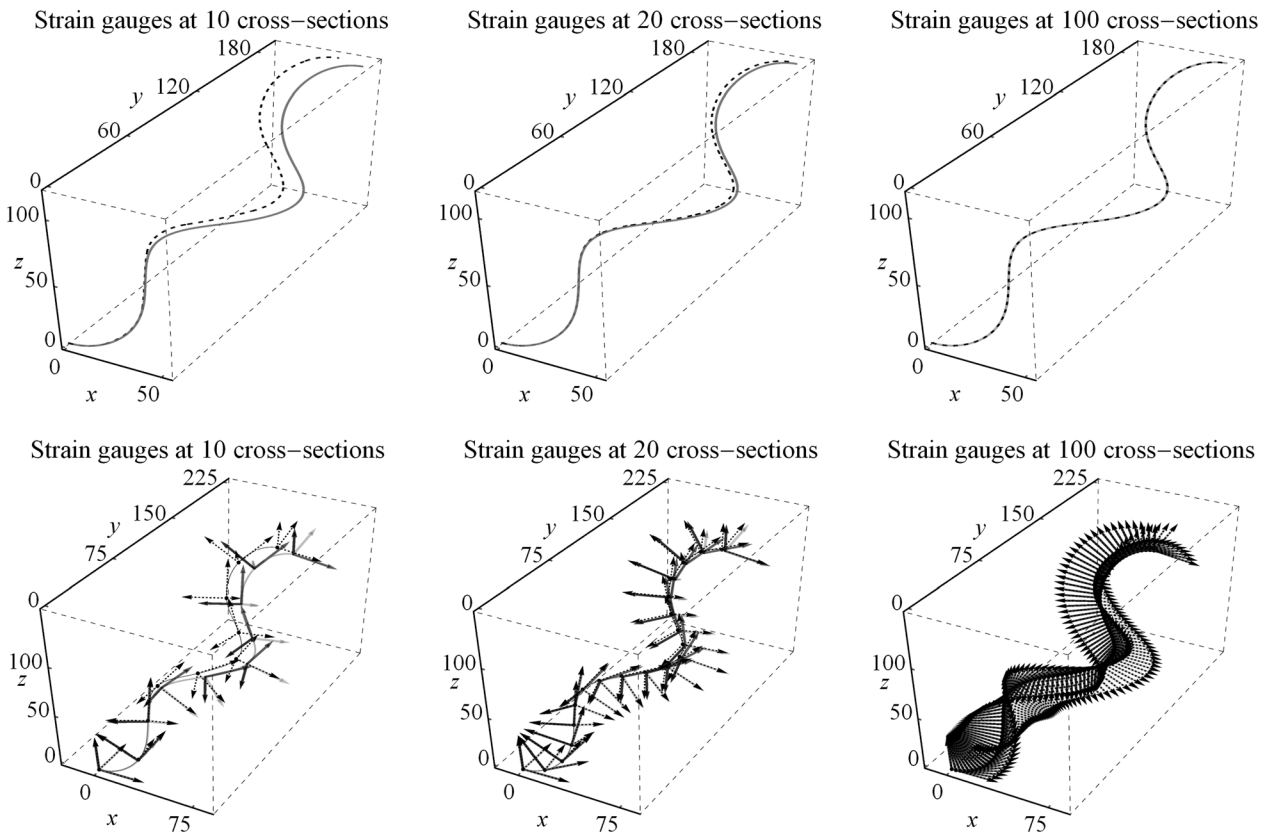

Fig. 6 Comparison of simulation 2 centerlines of exact (gray solid line) and reconstructed via strain (dashed lines) (top plots) and exact directors (d_1, d_2, and d_3 are represented by solid medium, light, and dark gray vectors, respectively) and the predicted directors (black-dashed directors) (bottom plots) of the object

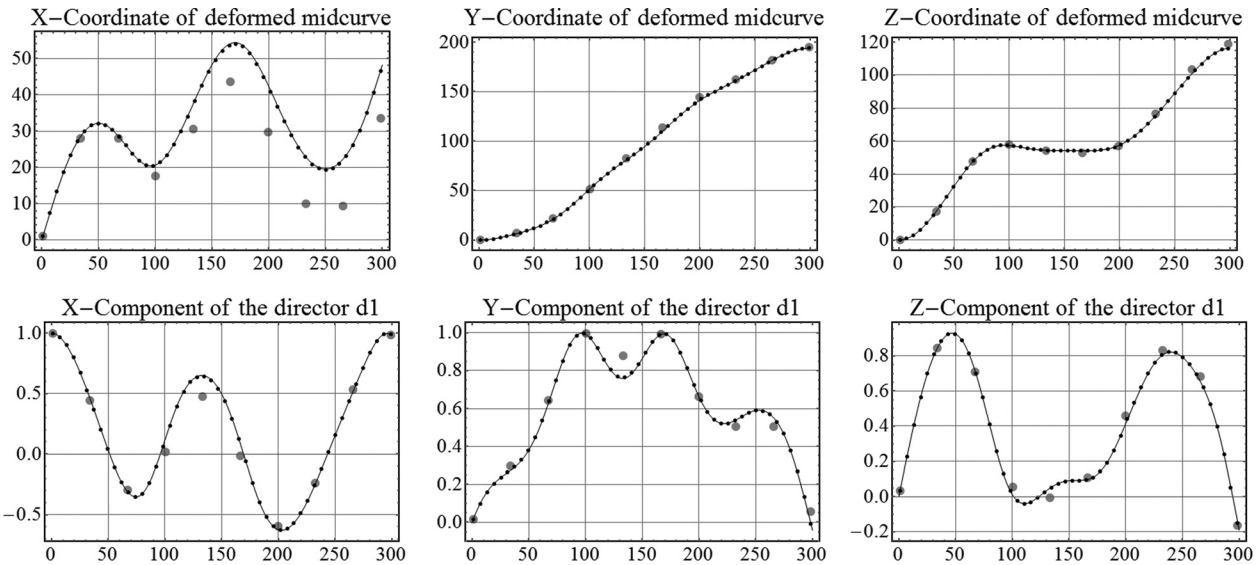

Fig. 7 Comparison of simulation 2 exact (black line) position vector components (top plots) and director d_1 components (bottom plots) with the predicted components for ten strain gauge locations (gray dots) and 50 strain gauge locations (black dots), where *x*-axis represents ξ_1

comparison of the exact component of $(\boldsymbol{\varphi}, \mathbf{d}_1)$ represented by solid black line with the components predicted by ten strain measurement locations (large gray dots) and 50 strain measurement locations (black dots). Assuming perfect strain transfer between the structure and the strain gauge (no noise and perfect bonding), exact and the predicted angles are observed to coincide because these parameters are directly related to the strain measurements.

The major contributor of error due to the algorithm, for this simulation, is mainly the deformed shape of the midcurve and the curvatures. The axial, shear, and torsion contributions are almost negligible to the rms error of the position vector to the midcurve. This observation is made clear from the rms error plot in Fig. 8. This is not a surprising result because the global shape of the structure in this example is still dominated by the curvature; in a simulation dominated by another effect, e.g., a pure axial extension, error would be primarily due to that instead, and using the simplified theory such as in Ref. [1] would induce significant error.

The same pattern of rms error is observed as in simulation 1 when external noise is added to the structure. The error is much higher for the second simulation as compared to the first because of complicated deformed shape of the midcurve and the complex curvature. As in Ref. [1], the maximum reconstruction error in both of the above simulations was observed at the distal end. The prime reason is because the boundary conditions were exactly specified on the proximal end. Error due to the algorithm itself (but not necessarily error due to external influence or measurement noise) then propagates along the object to the maximum at the far end from the known condition. Therefore, the error propagations start from the point of specified boundary condition.

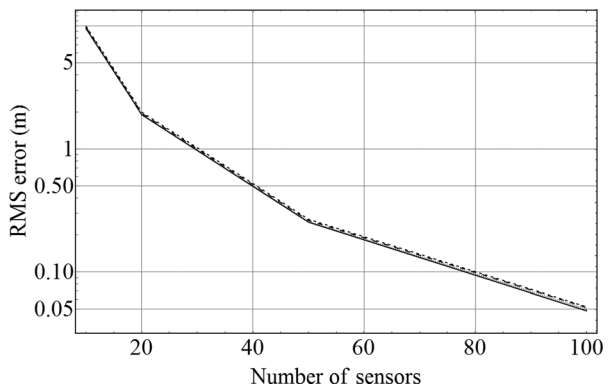

Fig. 8 Root mean square error for the position vector for simulation 2 with no noise, considering all the deformations (solid line), ignoring shear (large dashed line), ignoring shear and torsion (medium dashed line), and ignoring shear, torsion, and axial strain (dotted line)

3.3 Simulation 3. In most cable- or tetherlike structures, curvature is the dominant deformation. The third simulation represents a cable with same cross section as the previous simulations but with a total length of 6.3 km, bottom helix radius of 50 m, and 20 turns with varying curvature and pitch length. Significant rms error of 15.9 m was observed with 50 sensor locations (one in every 126 m) and it reduced to 0.78 m with 200 sensor locations (one cross section every 32 m). The predicted shape using 20 sensor locations was not acceptable with tremendous error of 1326 m because of complex shape and curvature changes. Figure 9 shows the predicted deformed shape and the directors for 50, 100, and 200 sensor locations. Figure 10 shows the comparison between the predicted components of the midcurve for 50 and 100 sensor locations as compared to the exact deformed shape. It is observed that an excellent reconstruction of such a complicated shape is observed with mere 200 sensor locations.

Furthermore, it is observed that for a constant radius and constant pitch spring, only two sensor locations (which is the minimum number of sensor locations required) are required to exactly predict the shape. Such a deformed shape is parameterized by constants $\bar{\kappa}_1$ and $\bar{\kappa}_2$ $(\bar{\kappa}_3 = \theta'(\xi_1) = 0)$ throughout the length of the cable.

4 Summary and Conclusions

This paper proposed a general method of three-dimensional shape reconstruction of slender structures. The work involved using the Cosserat beam theory to develop the equation of strain such that the effect of curvature ($\bar{\kappa}_2$ and $\bar{\kappa}_3$), torsion of the cross section ($\bar{\kappa}_1$), axial deformation of midcurve (e), and the shear of the cross section (γ_{11}, γ_{12}, and γ_{13}) are included. The theory uses the director mechanics in which the deformation of a three-dimensional slender object consists of the deformed midcurve and a triad of directors that describes the orientation of the cross

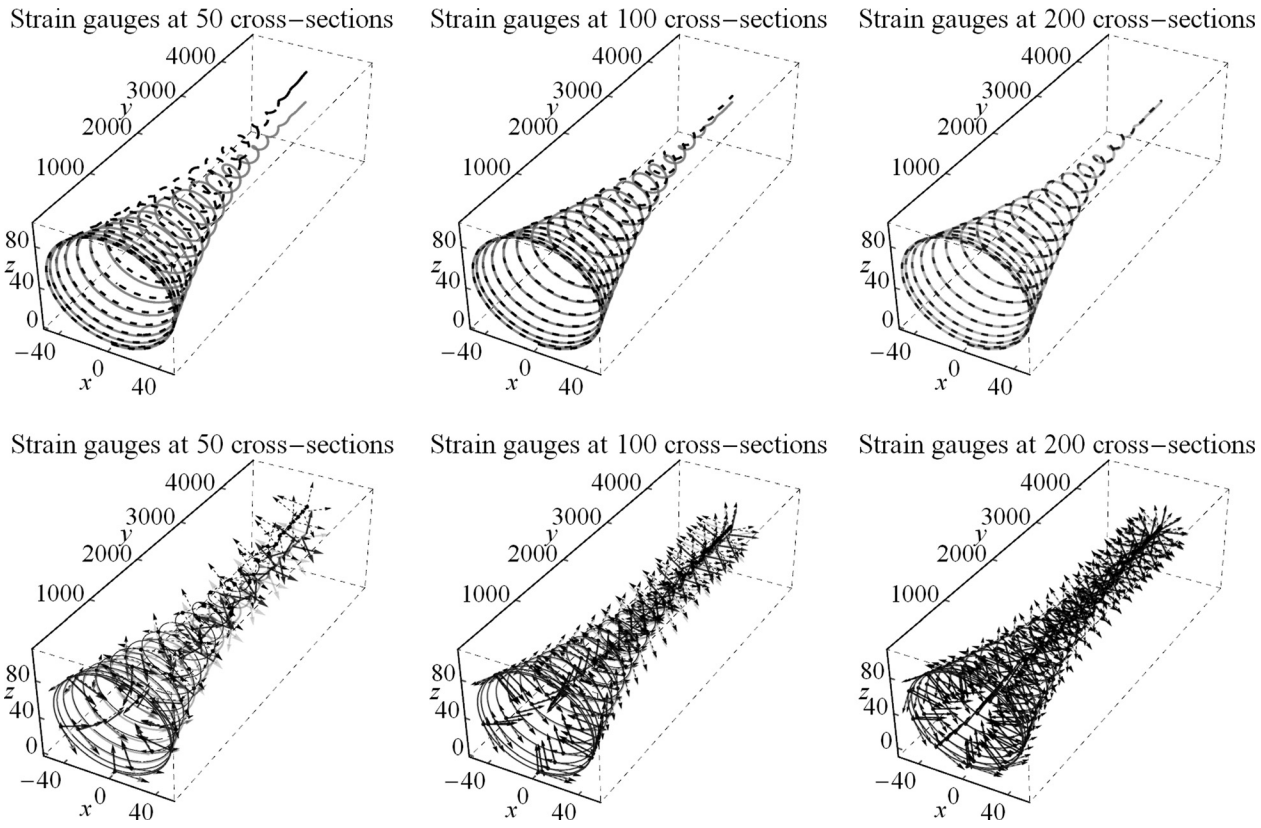

Fig. 9 Comparison of simulation 3 centerlines of exact (gray line) and reconstructed via strain (dashed line) (top plots) and exact directors (d_1, d_2, and d_3 are represented by solid medium, light, and dark gray vectors, respectively) and the predicted directors (black-dashed directors) (bottom plots) of the object

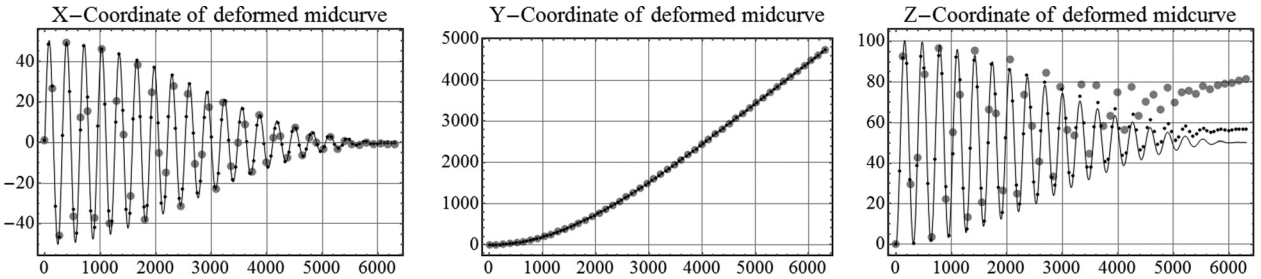

Fig. 10 Comparison of simulation 3 exact (black line) position vector components for 50 strain gauge locations (gray dots) and 100 strain gauge locations (black dots), where *x*-axis represents ξ_1

section at each midcurve point. The evolution of the position vector and the director with the undeformed arc-length is obtained using Cosserat theory, and a locally linearized form of those equations is solved exactly. The global solution to the deformed shape of the midcurve and the directors (and hence the cross section orientation) is obtained considering the continuity in the solution at the midpoint of each segment. The solution was shown to be robust in terms of predicting the deformed shape as well as the cross-sectional orientation. This approach being an extension of the shape sensing methodology presented in Ref. [1] also considers shear, torsion, and elongation, unlike Ref. [1], that only considered the curvature (which is the most dominant effect). This approach needs more strain measurements per cross section (six gauges) as compared to Ref. [1], where only three strain gauges were required, but this is expected because substantially more mechanics is engrained into the present formulation. The algorithm developed to solve for the shape using measured strains is a very simple operation, with most complex component being a matrix inversion. This algorithm could potentially be embedded in digital signal processing chips or field-programmable gate array as part of an embedded solution with low power and memory requirements.

The solution proposed here assumes a rigid cross section. A further extension to this theory can be proposed by including Poisson's effect and warping effects, but these effects do not affect the global deformation of slender objects, so they were ignored in this study. This approach is validated by comparing imposed solution cases with the predicted result from the algorithm developed. A 300 m long cable is subjected to torsion and curvature in simulation 1 and shear, torsion, elongation, and complex curvature in simulation 2. Simulation 3, run on a 6.3 km long cable, mainly concentrates on studying the effectiveness of the method to predict the reconstructed shape for a structure with complicated curvatures, such that other effects can be ignored. It is observed that the rms error mainly depends on the geometry and complexity of the deformed midcurve that is governed by the curvature. We observed that the rms error decays with increment of number of sensor points (for instance, 9.8 m using ten sensor

locations to 4.8 cm with 100 sensor locations for simulation 2). If the strain measurement is noise free and exact strain is captured by the strain gauge, exact shear angles, axial strains, and curvatures can be measured at that cross section. Preliminary noise tolerance study and boundary condition uncertainty studies show that the rms error trends with the extraneous noise due to environmental or measurement noise and with error in specifying the one boundary condition vector required for inertial reference.

Appendix

A.1 The Curvature Terms

The curvature terms $(\bar{\kappa}_1, \bar{\kappa}_2, \bar{\kappa}_3)$ in Eq. (10) are functions of the parameters γ_{11}, γ_{12}, γ_{13}, α_1, α_2, α_3, ϕ, θ, and their derivatives, given explicitly as

$$\begin{aligned}\bar{\kappa}_1 = {} & -\alpha_2' \cos\alpha_3 \sin\alpha_2 + \alpha_3' \cos\alpha_2 \sin\alpha_3 + \gamma_{11}' \cos\alpha_1 \sin\gamma_{11}(-\cos\alpha_3 \sin\gamma_{12} + \cos\alpha_2 \sin\gamma_{13}) \\ & -\gamma_{12}' \cos\alpha_2^2 \cos\gamma_{12} \sin\gamma_{13} - \gamma_{13}' \cos\gamma_{13} \sin\gamma_{13} + \gamma_{13}' \cos\alpha_3^2 \cos\gamma_{13} \sin\gamma_{12} \\ & -\gamma_{13}' \cos\alpha_2 \cos\alpha_3 \cos\gamma_{13} \sin\gamma_{13} + \theta'(\cos\alpha_3 \sin\gamma_{12} - \cos\alpha_2 \sin\gamma_{13}) - \phi'(\cos\alpha_1 \cos\theta + \cos\gamma_{11} \sin\theta)\end{aligned}$$

$$\begin{aligned}\bar{\kappa}_2 = {} & \frac{1}{2}\Big(2\alpha_1' \cos\alpha_3 \sin\alpha_1 - 2\alpha_3' \cos\alpha_1 \sin\alpha_3 + \gamma_{11}'\big(2 + \cos(2\alpha_2) + \cos(2\alpha_3)\big)\sin\gamma_{13} \\ & + \gamma_{12}'\big(\cos\alpha_1 \cos\alpha_3 \sin(2\ \gamma_{12}) + 2\cos\alpha_2 \cos\gamma_{12}(-\cos\alpha_3 \cos\gamma_{11} + \cos\alpha_1 \sin\gamma_{13})\big) \\ & + 2\big(\cos\gamma_{11} \cos\gamma_{13} \sin\alpha_3^2 + \cos\alpha_1 \cos\alpha_3 \sin(2\ \gamma_{13})\big) + 2\theta'(-\cos\alpha_3 \cos\gamma_{11} + \cos\alpha_1 \sin\gamma_{13}) - 2\phi'(\cos\alpha_2 \cos\theta + \sin\gamma_{12} \sin\theta)\Big)\end{aligned}$$

$$\begin{aligned}\bar{\kappa}_3 = {} & -\alpha_1' \cos\alpha_2 \sin\alpha_1 + \alpha_2' \cos\alpha_1 \sin\alpha_2 + \gamma_{12}'(\cos\alpha_1 \cos\alpha_3 \cos\gamma_{12} \sin\gamma_{13}) \\ & + \gamma_{11}' \cos\alpha_3 \sin\gamma_{11}(-\cos\alpha_3 \sin\gamma_{12} + \cos\alpha_2 \sin\gamma_{13}) - \gamma_{12}' \cos\alpha_3^2 \cos\gamma_{11} \cos\gamma_{12} \\ & + \gamma_{13}' \cos\alpha_2 \cos\alpha_3 \cos\gamma_{11} \cos\gamma_{13} - \gamma_{13}' \cos\alpha_1 \cos\alpha_3 \cos\gamma_{13} \sin\gamma_{12} \\ & + \theta'(\cos\alpha_2 \cos\gamma_{11} - \cos\alpha_1 \sin\gamma_{12}) - \phi'(\cos\alpha_3 \cos\theta + \sin\gamma_{13} \sin\theta)\end{aligned}$$

A.2 The Coefficients for the Position Vector of the Midcurve

The solution of four simultaneous differential equations in Eq. (18) yields the position vector of the midcurve and the directors at the cross section located at ξ_{1_n} as a function of the outer radius r and the strain parameters S_{l_n}, where $l = 1, \ldots, 6$. The vector constant terms for the position vector $\boldsymbol{\varphi}_n$ as represented in Eq. (19) are given below as

$$\mathbf{A}_{n,k} = \sum_{i=1}^{3}\left(\sum_{j=1}^{4} a_{n_{kj}} c_{nji}\right)\mathbf{E}_i$$

$$\mathbf{C}_{n,i} = c_{n_{ip}}\mathbf{E}_p \quad \text{where } p = 1, \ldots, 3 \text{ and } i = 1, \ldots, 4.$$

Terms corresponding to $\mathbf{A}_{n,1}$

$$a_{n_{11}} = \frac{r(S_{3n}S_{5n} - S_{2n}S_{6n})}{\gamma_n^2} + \frac{[S_{4n}(S_{2n}S_{5n} + S_{3n}S_{6n}) + (1 + S_{1n})S_{4n}^2]}{\gamma_n^2}\xi_1$$

$$a_{n_{12}} = \frac{r((1 + S_{1n})S_{6n} - S_{3n}S_{4n})}{\gamma_n^2} + \frac{[S_{5n}((1 + S_{1n})S_{4n} + S_{3n}S_{5n}S_{6n})]}{\gamma_n^2}\xi_1$$

$$a_{n_{13}} = \frac{r(S_{2n}S_{4n} - S_{5n}(1 + S_{1n}))}{\gamma_n^2} + \frac{[S_{4n}S_{6n}(1 + S_{1n}) + S_{6n}(S_{2n}S_{5n} + S_{3n}S_{6n})]}{\gamma_n^2}\xi_1$$

$$a_{n_{14}} = 1$$

Terms corresponding to $\mathbf{A}_{n,2}$

$$a_{n_{21}} = \frac{r}{\gamma_n^3}\left[-S_{2n}S_{4n}S_{5n} + (1 + S_{1n})S_{5n}^2 + S_{6n}(-S_{3n}S_{4n} + (1 + S_{1n})S_{6n})\right]$$

$$a_{n_{22}} = \frac{r}{\gamma_n^3}\left[-S_{5n}((1 + S_{1n})S_{4n} + S_{3n}S_{6n}) + S_{2n}\left(S_{4n}^2 + S_{6n}^2\right)\right]$$

$$a_{n_{23}} = \frac{r}{\gamma_n^3}\left[\left(S_{3n}\left(S_{4n}^2 + S_{5n}^2\right) - ((1 + S_{1n})S_{4n} + S_{2n}S_{5n})S_{6n}\right)\right]$$

$$a_{n_{24}} = 0$$

Terms corresponding to $\mathbf{A}_{n,3}$

$$a_{n_{31}} = \frac{r}{\gamma_n^2}\left[-S_{3n}S_{5n} + S_{2n}S_{6n}\right]$$

$$a_{n_{32}} = \frac{r}{\gamma_n^2}\left[S_{3n}S_{4n} - (1 + S_{1n})S_{6n}\right]$$

$$a_{n_{33}} = \frac{r}{\gamma_n^2}\left[-S_{2n}S_{4n} + (1 + S_{1n})S_{5n}\right]$$

$$a_{n_{34}} = 0$$

References

[1] Todd, M. D., Skull, C. J., and Dickerson, M., 2013, "A Local Material Basis Solution Approach to Reconstructing the Three-Dimensional Displacement of Rod-Like Structure From Strain Measurements," ASME J. Appl. Mech., **80**(4), p. 041028.

[2] Shield, R. T., and Im, S., 1986, "Small Strain Deformations of Elastic Beams and Rods Including Large Deformations," J. Appl. Math. Phys., **37**(4), pp. 491–513.

[3] Iura, M., and Atluri, S. N., 1989, "On a Consistent Theory, and Variational Formulation of Finitely Stretched and Rotated 3-D Space-Curved Beam," Comput. Mech., **4**(2), pp. 73–88.

[4] Simo, J. C., and Vu-Quoc, L., 1991, "A Geometrically Exact Rod Model Incorporating Shear and Torsion-Warping Deformation," Int. J. Solids Struct., **27**(3), pp. 371–393.
[5] Reissner, E., 1972, "On One-Dimensional Finite-Strain Beam Theory: The Plane Problem," J. Appl. Math. Phys., **23**(5), pp. 795–804.
[6] Reissner, E., 1973, "On One-Dimensional Large Displacement Finite Beam Theory," Stud. Appl. Mech., **52**(2), pp. 87–95.
[7] Reissner, E., 1981, "On Finite Deformation of Space Curved Beams," J. Appl. Math. Phys., **32**(6), pp. 734–744.
[8] Love, A. E. H., 1944, *A Treatise on Mathematical Theory of Elasticity*, 4th ed., Dover, New York.
[9] Cosserat, E., and Cosserat, F., 1909, *Theorie des Corps Deformable*, Herman, Paris, France.
[10] Rubin, M. B., 1985, "On the Numerical Solution of One-Dimensional Continuum Problems Using the Theory of a Cosserat Point," ASME J. Appl. Mech., **52**(2), pp. 373–378.
[11] Rubin, M. B., 1985, "On the Theory of a Cosserat Point and Its Application to the Numerical Solution of Continuum Problems," ASME J. Appl. Mech., **52**(2), pp. 368–372.
[12] Rubin, M. B., 2000, *Cosserat Theories: Shells, Rods and Points*, Kluwer Academic Publishers, Dordrecht, The Netherlands.
[13] Todd, M. D., Mascarenas, D., Overbey, L. A., Salter, T., Baldwin, C., and Kiddy, J., 2005, "Towards Deployment of a Fiber Optic Smart Tether for Relative Localization of Towed Bodies," SEM Annual Conference on Experimental Mechanics, Portland, OR, June 6–9.
[14] Friedman, A., Todd, M. D., Kirkendall, K., Tveten, A., and Dandridge, A., 2003, "Rayleigh Backscatter-Based Fiber Optic Distributed Strain Sensor With Tunable Gage Length," SPIE Smart Structures/NDE 5050 Proceedings, San Diego, CA, Mar. 2–6.
[15] Duncan, R., Froggatt, M., Kreger, S., Seeley, R., Gifford, D., Sang, A., and Wolfe, M., 2007, "High-Accuracy Fiber Optic Shape Sensing," SPIE Smart Structures/NDE 6530 Proceedings, San Diego, CA, Mar. 19–22.
[16] Li, J., 2000, "A Geometrically Exact Curved Beam Theory and Its Finite Element Formulation/Implementation," Master thesis, Virginia Polytechnic Institute and State University, Blacksburg, VA.
[17] Argyris, J., 1982, "An Excursion Into Large Rotations," Comput. Methods Appl. Mech. Eng., **32**(1–3), pp. 85–155.